SANDIA REPORT
SAND2021-14588
Printed November, 2021

Sandia National Laboratories

Soot Predictions with a Laminar Flamelet Combustion Model in SIERRA/Fuego on a Coflow Scenario

Andrew Kurzawski, Michael Hansen, John Hewson

Prepared by
Sandia National Laboratories
Albuquerque, New Mexico 87185
Livermore, California 94550

Issued by Sandia National Laboratories, operated for the United States Department of Energy by National Technology & Engineering Solutions of Sandia, LLC.

Available to DOE and DOE contractors from

U.S. Department of Energy
Office of Scientific and Technical Information
P.O. Box 62
Oak Ridge, TN 37831

Telephone: (865) 576-8401
Facsimile: (865) 576-5728
E-Mail: reports@osti.gov
Online ordering: http://www.osti.gov/scitech

Available to the public from

U.S. Department of Commerce
National Technical Information Service
5301 Shawnee Road
Alexandria, VA 22312

Telephone: (800) 553-6847
Facsimile: (703) 605-6900
E-Mail: orders@ntis.gov
Online order: https://classic.ntis.gov/help/order-methods

ABSTRACT

This report describes an assessment of flamelet based soot models in a laminar ethylene coflow flame with a good selection of measurements suitable for model validation. Overall flow field and temperature predictions were in good agreement with available measurements. Soot profiles were in good agreement within the flame except for near the centerline where imperfections with the acetylene-based soot-production model are expected to be greatest. The model was challenged to predict the transition between non-sooting and sooting conditions with non-negligible soot emissions predicted even down to small flow rates or flame sizes. This suggests some possible deficiency in the soot oxidation models that might alter the amount of smoke emissions from flames, though this study cannot quantify the magnitude of the effect for large fires.

ACKNOWLEDGMENT

The authors would like to thank Joshua Hubbard and Alexander Brown for their thoughtful reviews of this report.

CONTENTS

LIST OF FIGURES

1. INTRODUCTION

Thermal radiation from soot is typically the most important cause of both fuel vaporization and thermal damage to the surroundings for large scale (> 1 m) fires. When more fuel is vaporized, a fire will release more heat and grow so that thermal radiation can potentially have a feedback effect. However, soot also absorbs radiant flux so that the presence of large quantities of soot observed in most fires acts both to emit and absorb thermal radiation.

The physics of soot formation, growth and oxidation remains a research challenge even for laminar flames. However, in these simpler flames it is possible to identify trends that are relevant to large fires where additional complications arise from turbulence and radiation interactions [23–25, 31]. One trend of interest is the tendency for larger fires and larger laminar flames in the configuration studied here to emit smoke [4, 18, 29]. It has been observed that for coflow flames there is a flame length (and equivalently a fuel mass flux) where there is a transition from a non sooting flame to one where soot is emitted in significant quantities. This is referred to as the smoke point [4, 18, 23, 24, 29], and this report considers conditions above and below the smoke point. The smoke point has been identified as a key metric for assessing soot predictions capabilities.

Measurements in large scale fires are particularly challenging because high levels of soot and radiation make optical and other measurements difficult. Most available measurements effectively average over a broad range of states. When available, point measurements in turbulent flames of soot and temperature occur over a distribution of mixing states so that results show a broad distribution of states [15, 20]. Heat flux measurements are averaged along lines of sight and also in time.

Recently, there has been a move toward soot models in fire environments that can adapt to different fuels [7, 8]. One approach that enables this is by pre-computing the detailed flame chemistry using flamelet approaches and using the results to provide soot source terms in fire simulations [10]. The flame chemistry and soot source terms in the flamelet calculations can employ a range of models available from the scientific literature. A benefit of this approach is that as improvements in the science of fuel chemistry and soot formation are published in the scientific literature, it is relatively easy to adopt these improvements into fire-scale predictions, nominally without the extensive calibration usually employed for soot modeling in fires [28].

In this report, we assess the performance of a set of models that has been employed to predict soot formation and oxidation in a range of external studies [5, 6, 10, 13, 19, 30, 32]. These models evolve two transport equations for soot, the number of soot particles and the overall mass conversion to soot, using source terms that are empirical but that take advantage of detailed chemical models to predict soot precursors. For the models addressed in this report, acetylene is the soot precursor for both nucleation and growth processes while oxidation by oxygen molecules

and OH radicals is included. In this manner, there is an interaction between the fuel chemistry predictions of the precursors and the soot production that should be assessed over a range of conditions.

The target configuration used in this work for assessing model performance is a laminar coflow configuration where fuel issues vertically into a chimney with air coflowing around the fuel. This creates what appears to be a large candle flame. The laminar coflow configuration in this report is based on the work of Santoro et al. [23, 24], and a variety of detailed experimental measurements are available in literature. Fuel and air flow rates in this dataset span the transition from non sooting to sooting flames. These experiments have been used in a variety of soot model validation studies, typically without employing laminar flamelet models [12, 16, 17].

The conditions vary from the base of the flame to the tip, providing a good test of model performance. At the base of the flame, the fuel-air mixing is fast and radiative cooling is small. Conversely, at the flame tip the fuel-air mixing is slow and radiative cooling is substantial. The flame length and thus the overall fuel-air mixing time at the flame tip varies with the fuel flow rate, adding another dimension to the test.

This report outlines the flamelet calculations, soot model, and computational domain for the coflow configuration. Simulation results are used to draw comparisons to experimental data. Analysis of the trends observed in the predictions is conducted using comparisons between 2-D axi-symmetric and 3-D simulations, post-processed integrated quantities, and simulations with a thermophoretic soot transport model.

2. METHODS

Simulations of bench-scale, ethylene co-flow flames were conducted in Sandia's low-Mach combustion module, SIERRA/Fuego version 4.57 [27]. This software simulates buoyantly-driven incompressible flow, heat transfer, combustion, and soot and is aimed at modeling large-scale fires. The choice of combustion model is key to the prediction of fire behavior, and in this work we examine the predictive capabilities of strained laminar flamelet models as implemented in Fuego by comparison to well characterized co-flow experimental data. The key components of this analysis are the construction of the flamelet model, the choice of chemical mechanism, the experimental datasets, and the discretization of the computational domain.

2.1. Experimental Validation Data

For this study, two ethylene co-flow flame datasets from Santoro et al. [23, 24] were chosen for their detailed soot and velocity measurements. The burner in these studies was constructed from concentric brass tubes with a fuel outlet diameter of 1.11 cm and air co-flow diameter of 10.16 cm. The chimney that contains the flame was 40.5 cm long with a flow restrictor at the top to prevent recirculation.

Two experimental conditions were chosen based on soot production to test soot model predictions. Santoro refers to these conditions as "NS" and "S" for non-sooting and sooting, respectively. The fuel and air flow velocities for these cases are listed in Table 2-1. Experimental measurements of particular interest for this work are the soot volume fraction, flow velocity, and temperature.

Table 2-1. Flow conditions for selected experiments from Santoro et al. [23, 24].

Case	Fuel Velocity (cm/s)	Air Velocity (cm/s)
NS	3.98	8.9
S	5.06	13.3

Soot volume fraction was quantified using laser light extinction and scattering measurements. Data were gathered in the radial direction from the center of the burner to beyond the edge of the flame at a range of heights above the burner. These radial profiles were integrated at each height to track total soot volume fraction versus height.

A laser velocimeter was used to collect velocity measurements as a function of radial position at a set of axial locations. The air and fuel were seeded with aluminum oxide particles to obtain laser velocimetry measurements. Temperature measurements were obtained by Type S thermocouples with a bead diameter of approximately 200 μm. The original study authors caution that these

thermocouple measurements should be interpreted qualitatively due to the difficulty of acquiring good measurements in a flame. They note that while the measurements have been corrected for radiative losses, conduction losses down the thermocouple leads have not been accounted for [24].

2.2. Predicting flame chemistry

In non-premixed combustion as occurs in fires, it is observed that the thermochemical state is most strongly correlated with the overall fraction of the fluid that originated in the fuel stream. Additional important correlations also occur depending on the mixing time scales and any heat losses. In flamelet approaches employed here, a large number of one-dimensional "flamelet" simulations describing the fuel-air mixing are conducted for a range of mixing time scales and heat loss rates. The fuel-air mixing is characterized using a mixture fraction variable, Z, that represents the fraction of the fluid originating in the fuel stream. In the CFD simulation, a transport equation for the mixture fraction along with equations for the enthalpy and soot quantities (mass of soot and moles of particles) are evolved in addition to the momentum and continuity. The full thermochemical state including source terms for soot production and consumption plus radiative emission and absorption source terms are then obtained from the flamelet results that are tabulated ahead of time.

To compute the flamelet quantities in a generalized manner, the species and energy transport equations are transformed into the mixture-fraction coordinate resulting in equations of the form

$$\frac{\partial Y_i}{\partial t} = \frac{\chi}{2}\frac{\partial^2 Y_i}{\partial Z^2} + \frac{\omega_i}{\rho}, \tag{2.1}$$

$$\begin{aligned}\frac{\partial T}{\partial t} = & -\frac{1}{\rho c_p}\sum_{i=1}^{n_s}\omega_i h_i + \frac{\chi}{2}\left(\frac{\partial^2 T}{\partial Z^2} + \frac{1}{c_p}\frac{\partial T}{\partial Z}\frac{\partial c_p}{\partial Z} + \frac{\partial T}{\partial Z}\sum_{i=1}^{n_s}\frac{c_{p,i}}{c_p}\frac{\partial Y_i}{\partial Z}\right) \\ & -\frac{H\chi_{\max}}{\rho c_p}\frac{1}{(1-Z_{st})Z_{st}}\frac{T-T_\infty}{T_{\max}(t)-T_\infty},\end{aligned} \tag{2.2}$$

wherein Y_i, h_i, $c_{p,i}$, and ω_i are the mass fraction, enthalpy, isobaric specific heat capacity, and net mass production rate of species i, respectively. T is the temperature, t is the flamelet evolution time, ρ is the mass density, c_p is the isobaric specific heat capacity of the mixture, T_∞ is a chosen cooled reference temperature, and H is an arbitrary heat transfer coefficient, discussed further below. The link between the mixture fraction coordinate and diffusive mixing rates occurs through the scalar dissipation rate, $\chi = 2D|\nabla Z|^2$ where D is a diffusion coefficient for fuel-air mixing obtained from a unity Lewis number approximation and the thermal diffusivity.

Flamelet profiles are created by first computing steady state flamelets with H set to zero (adiabatic flames) for a large range of scalar dissipation rates (stoichiometric values from $\chi_{st} = 10^{-3}\,\mathrm{s}^{-1}$ to $\chi_{st} = 1200\,\mathrm{s}^{-1}$). Using these steady-state adiabatic profiles, the heat loss coefficient is set to $H = 8\times10^5\,\mathrm{W/m^3}$ leading to flame cooling at a rate commensurate with radiative cooling. This rate of cooling causes the flame state to evolve through extinction by cooling (simulating radiative quenching) down to near ambient temperatures [10].

2.3. Conservation equations for coflow flame structure

The co-flow scenario is a controlled laminar diffusion flame which is not typical of the large, turbulent fire environments that are studied with Fuego. The laminar flow equations for mass, momentum, energy, and scalar transport are solved in Fuego while the method for solving radiation transport is dependent on the computational domain. For a 2-dimensional axi-symmetric domain, a simple radiation source is modeled in Fuego that approximates radiative heat transfer as the difference between the local temperature to the fourth power and a reference temperature to the fourth power. For the 3-dimensional simulations, radiation transport is solved using discrete ordinates with quadrature order 3 via coupling to Nalu [11]. For brevity, details of the mass, momentum, and energy equations can be found in the Fuego theory manual [26], and the conservation of mixture fraction and soot will be described in this section.

Conservation of the mixture fraction, Z, is given as

$$\frac{\partial(\rho Z)}{\partial t} + \frac{\partial(\rho Z u_j)}{\partial x_j} = \frac{\partial}{\partial x_j}\left(\frac{\mu}{\mathrm{Sc}_s}\frac{\partial Z}{\partial x_j}\right) - \dot{\omega}^{Y_s}, \tag{2.3}$$

where $\dot{\omega}^{Y_s}$ is the soot mass fraction source term given below, ρ is the gas density, μ is the gas viscosity, u_j is the velocity in the j direction, and Sc_s is the soot Schmidt number. In this approach the soot is not included in the mixture fraction because slow soot evolution relative to fuel-air mixing means that soot is not well correlated with the mixture fraction like the main flame chemistry is. The soot Schmidt number is 200 in this work, resulting in negligible soot diffusion relative to the diffusion of other scalars, the mixture fraction and enthalpy.

Soot is modeled with a two-equation formulation where transport equations are solved for the soot number density, N_s, and the soot mass fraction, Y_s. Empirical source terms as a function of the temperature and acetylene concentration are obtained from literature models [1, 2, 6], and the inputs for these models are obtained from flamelet libraries.

The conservation of soot mass fraction is given by

$$\frac{\partial(\rho Y_s)}{\partial t} + \frac{\partial(\rho Y_s u_j)}{\partial x_j} = \frac{\partial}{\partial x_j}\left(\frac{\mu}{\mathrm{Sc}_s}\frac{\partial Y_s}{\partial x_j}\right) + \dot{\omega}^{Y_s}. \tag{2.4}$$

where the source term, $\dot{\omega}^{Y_s}$, is expressed in terms of four sources: nucleation, surface growth, and OH and O_2 oxidation.

$$\begin{aligned} \dot{\omega}^{Y_s} \;=\; & \dot{\omega}_R W_p A_N [\mathrm{C_2H_2}] \exp\left(-T_N/T\right) \\ & + \Big[\dot{\omega}_R A_{SG} [\mathrm{C_2H_2}] \exp\left(-T_{SG}/T\right) \\ & - A_{\mathrm{O_2}} [\mathrm{O_2}] \sqrt{T} \exp\left(-T_{\mathrm{O_2}}/T\right) \\ & - A_{\mathrm{OH}} [\mathrm{OH}] \sqrt{T}\Big] v_d^2 \pi \rho Y_s^{2/3} N_s^{1/3}, \end{aligned} \tag{2.5}$$

where the molecular weight of a soot nucleate, W_p, is taken as the molecular weight of twelve carbon atoms, giving 144 kg/kmol. Surface growth (SG) and oxidation rate coefficients are $A_{SG} = 11{,}700\ \mathrm{s}^{-1}$, $T_{SG} = 12{,}000$ K, $A_{O_2} = 500\ \mathrm{s}^{-1}$, $T_{O_2} = 21{,}000$ K, and $A_{OH} = 4.23\ \mathrm{s}^{-1}$.

The conservation of soot moles per mass is given as

$$\frac{\partial(\rho N_s)}{\partial t} + \frac{\partial(\rho N_s u_j)}{\partial x_j} = \frac{\partial}{\partial x_j}\left(\frac{\mu}{\mathrm{Sc}_s}\frac{\partial N_s}{\partial x_j}\right) + \dot{\omega}^{N_s}, \tag{2.6}$$

with the source term $\dot{\omega}^{N_s}$ modeled as

$$\dot{\omega}^{N_s} = \overline{\dot{\omega}_R A_N [C_2H_2] \exp\left(-T_N/T\right)} - \overline{\sqrt{\frac{24 v_d R T N_A}{\rho_{soot}}}\rho^2 Y_s^{1/6} N_s^{11/6}}, \tag{2.7}$$

where the first term on the right-hand side represents nucleation, and the second term represents coagulation as derived from particle collision theory as described by Smoluchowski. The nucleation rate is governed by an Arrhenius rate model with a pre-exponential coefficient $A_N = 54\ \mathrm{s}^{-1}$, and an activation temperature $T_N = 21{,}100$ K (175 kJ mol^{-1}). This rate is proportional to the acetylene concentration, $[C_2H_2]$ in kmol kg^{-1}.

The second term represents coagulation in the free molecular limit where $\rho_{soot} = 1800$ kg/m^3 is the soot density and N_A is Avagadro's number. The constant $v_d = [6/(\pi\rho_{soot}N_A)]^{1/3}$ is used in converting the particle volume to its diameter, assuming all particles are of uniform size. Particles are treated as spherical to estimate coagulation; fractal aggregates tend to have larger cross-sectional areas and agglomerate faster, reducing the particle number density, but the spherical assumption might adequately represent the primary particle surface area, providing a reasonable estimate of overall mass growth and soot volume fraction required for radiation source term estimates.

One modification needed for the source terms in large turbulent fires is retained here: in the core regions of the fire, rich soot laden mixtures can absorb radiant energy and remain quite hot. Because soot formation in these two equation models follows a simple Arrhenius rate, elevated temperatures lead to unphysically large soot production rates. It is known that soot growth follows a so-called bell curve (e.g., [3, 14]) where molecular decomposition inhibits soot growth at high temperatures. To mimic this, we introduce one additional term, $\dot{\omega}_R$, that smoothly adjusts the soot nucleation and surface growth to a negative value above temperatures of T_c; the rate of this transition is given by an effective decomposition activation temperature, T_R.

$$\dot{\omega}_R = 1 - \exp\left(T_R\left(\frac{1}{T_c} - \frac{1}{T}\right)\right) \tag{2.8}$$

2.4. Computational Domain

Two computational domains were generated for simulation in Fuego: a 2-D axi-symmetric domain and a 3-D domain. Figure 2-1 outlines the features of these domains including: dimensions, inflow/outflow locations, axes, and a notional flame. In each domain, a 20 cm tall fuel inlet section is modeled to provide sufficient time for development of the flow. The fuel inflow radius, air inflow radius, and chimney height follow the experimental dimensions with the exception of the 3-D case where a flow restrictor was added to the top of the chimney. The flow restrictor decreases the outlet diameter by 1/2 and has a height of 2.54 cm which helps to prevent recirculating flow and improves numerical stability.

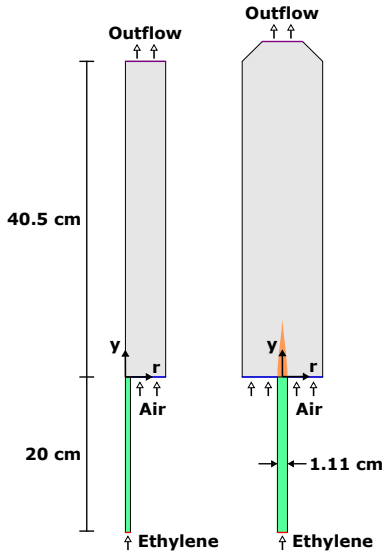

Figure 2-1. 2-D axi-symmetric simulation domain (left) and a vertical slide of the 3-D domain (right).

The 2-D mesh contains 98,010 nodes and is discretized in to quadrilateral elements. The fuel inflow section has 20 elements across the radius (r_f) and with a constant axial discretization of r_f/10. Discretization of the chimney in the axial (y) direction grows uniformly from r_f/20 at the base of the chimney (y = 0 cm) to r_f/5 at the outlet (y = 40.5 cm). In the core of the chimney where r is less than r_f, the radial discretization is constant, and outside of this core the element size grows evenly from r_f/20 to r_f/10. A close-up of the connection between the fuel inlet and chimney can be seen in Figure 2-2 left.

The 3-D domain is discretized with hexahedral elements and a total of 882,223 nodes. The discretization in the axial (y) and radial (r) directions is coarser than the 2-D domain. Inside the fuel inlet, the maximum axial and radial discretization is r_f/10 with a finer "paved" mesh at the core of the inlet (see Fig 2-2 right). Inside the chimney section, the axial discretization grows evenly to r_f/2.5 at the outlet which includes the flow restrictor (y = 43.4 cm), while the radial discretization grows from r_f/10 at $r = r_f$ to r_f/2.5 at r = 5.08 cm. Similar to the 2-D domain, the radial discretization in the core of the flow ($r < r_f$) is constant in the chimney section. Finally, the azimuthal direction is discretized in to 32 elements.

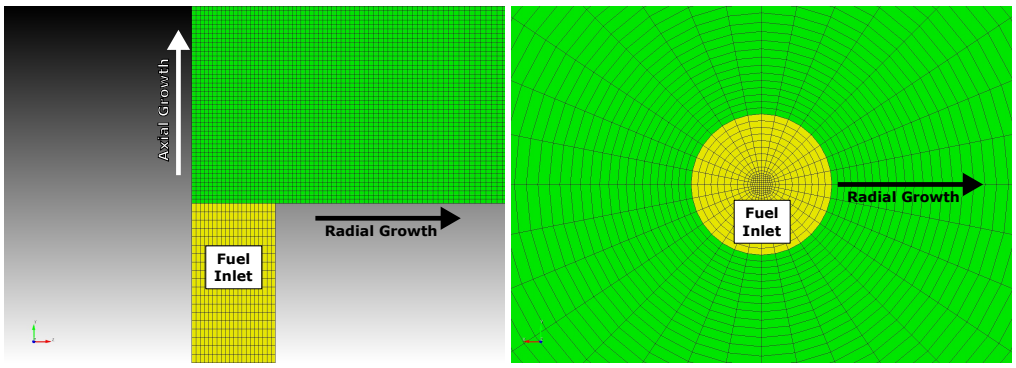

Figure 2-2. 2-D axi-symmetric simulation mesh at the connection between the fuel inlet and chimney (left) and a bottom view of the 3-D mesh (right).

2.5. Scaling analysis for coflow flames

In this section we introduce some basic scale relationships for coflow laminar diffusion flames. If the conservation equations are written in axi-symmetric form and integrated over the flow area following Peters and Göttgens [21] several of the terms cancel out. The area-integrated axial momentum, mixture fraction, enthalpy, and soot mass fraction equations are

$$\frac{\partial}{\partial y}\int_0^\infty \pi\rho u^2 r dr + u_\infty \frac{\partial}{\partial y}\int_0^\infty \rho u r dr = \frac{\partial}{\partial y}\pi\hat{\rho}\hat{u}^2 b^2 = \int_0^\infty \pi(\rho_\infty - \rho) g r dr, \tag{2.9}$$

$$\frac{\partial}{\partial y}\int_0^\infty \pi\rho u Z r dr = \frac{\partial}{\partial y}\pi\hat{\rho}\hat{u}\hat{Z} b^2 = -\int_0^\infty \pi\dot{\omega}^{Y_s} r dr \tag{2.10}$$

$$\frac{\partial}{\partial y}\int_0^\infty \pi\rho u (Z + Y_s) r dr = \frac{\partial}{\partial y}\pi\hat{\rho}\hat{u}(\hat{Z} + \hat{Y}_s) b^2 = 0 \tag{2.11}$$

$$\frac{\partial}{\partial y}\int_0^\infty \pi\rho u h r dr = \frac{\partial}{\partial y}\pi\hat{\rho}\hat{u}\hat{h} b^2 = \int_0^\infty \pi\left(4\sigma\overline{\alpha T^4} - \overline{\alpha G}\right) r dr, \tag{2.12}$$

$$\frac{\partial}{\partial y}\int_0^\infty \pi\rho u Y_s r dr = \frac{\partial}{\partial y}\pi\hat{\rho}\hat{u}\hat{Y}_s b^2 = \int_0^\infty \pi\dot{\omega}^{Y_s} r dr. \tag{2.13}$$

In these expressions, b represents a width of the flow, relatively constant but slightly contracting in buoyant coflow flames [22]. Variables with a carat on top represent characteristic values of the various variables appropriately adjusted with b to match the initial conditions and integrated source terms. Note that α in the area-integrated enthalpy equation is the absorption coefficient in units of 1/m, and the source terms ($\dot{\omega}$) are per unit volume.

Equation 2.9 shows how the flow momentum increased due to entrainment of the coflow and more significantly due to buoyant acceleration. The buoyant acceleration can be used to estimate the characteristic vertical velocity, $\hat{u}$, as

$$\hat{u} = \sqrt{u_0^2 + ay} \qquad \text{where} \qquad a = \frac{1}{\rho_\infty b^2}\int_0^\infty (\rho_\infty - \rho) g r dr, \tag{2.14}$$

with a being the bulk vertical acceleration of the flow in the flame. Roper demonstrated that the flame height, H, scales with the volumetric flow rate divided by the diffusivity, $H \propto \dot{V}/D$ where

$\dot{V} = u_o d_0^2$ is the volumetric flow rate [22]. In this report, we introduce $\eta = yD/\dot{V}$ as a dimensionless axial coordinate. Santoro et al. found that flame heights for ethylene flames are approximately $\eta = 0.36$ so that the flame height is $H = 0.36\dot{V}/D$ [24]. The time for the flow to reach H, the flow residence time, is

$$t_{res} = \int_0^H \frac{dy}{\sqrt{u_0^2 + ay}} = \frac{2}{a}\sqrt{u_0^2 + 0.36a\dot{V}/D} \tag{2.15}$$

We will see that the buoyant acceleration is much greater than the initial momentum so that the total flame residence time can be estimated to be $t_{res} \approx \sqrt{4 \times 0.36\dot{V}/(aD)}$. For a given distance represented in terms of x or η the residence time is approximately

$$t_{res} \approx \sqrt{\frac{4y}{a}} = \sqrt{\frac{4\eta\dot{V}}{aD}} \tag{2.16}$$

Neglecting the variation in the buoyant acceleration and the diffusivity across different flame cases, the residence time is proportional to the square root of the volumetric flow rate. Because soot formation and radiative losses are both slow relative to the fuel air mixing that determines the residence time, flames with greater residence times will undergo greater soot formation and greater radiative losses; these are flames with larger volumetric flow rates. This fact is important in interpreting the behavior of the various flames studied in this report.

3. RESULTS AND ANALYSIS

Simulations were conducted on the non-sooting and sooting flames for both 2-D axi-symmetric and 3-D domains. This chapter presents a characteristic set of predictions and proceeds to comparisons of simulations and experimental measurements, focusing on the 2-D axi-symmetric domain. Model verification is conducted with the 3-D simulations. Additional in-depth analysis is conducted through examination of various integral quantities to understand the soot model predictions, and a thermophoretic soot transport model is presented in an effort to improve the predictive capabilities of the simulations.

3.1. Results

Figure 3-1 provides contour plots of the temperature and velocity fields for the flame referred to as S in Table 2-1. This flame is one where soot is observed to be emitted from the tip of the flame; it is above the laminar smoke point [18]. The high temperature region closes gradually at a height of 80 to 100 mm (roughly eight to ten jet diameters) while the axial velocity gradually increases due to buoyancy. With the acceleration of the vertical flow, streamlines converge slightly so that radial spreading is minimal even with the effects of viscosity and diffusivity. This is characteristic of streamlines predicted by early analyses of coflow diffusion flames such as those of Roper [22]. These contours show that the highest temperature regions near the flame tip have cooled somewhat relative to the annular flame temperatures in the first half of the flame height. This cooling will be associated with radiative emissions as discussed below.

Figure 3-2 shows contours of the soot mass fraction and its source terms with overlaid streamlines according to predictions. Soot exists in a thin layer on the fuel-rich side of the highest temperature (stoichiometric) regions. For this flame above the smoke point, a trail of soot is observed to be emitted from the flame in a narrow annulus at the flame tip.

Soot source terms in Figure 3-2 show the predominance of a positive soot source up to approximately 45 mm, or nearly half of the temperature-based flame height. Above this the overall source terms are negative and soot oxidation is dominant. In the lower portion of this flame the convergence of the streamlines with buoyant acceleration together with the outward diffusion of the fuel cause produced soot to be advected away from the highest temperature regions making oxidation difficult. In the upper half of the flame the direction of flame diffusion shifts as the centerline fuel is diluted by products so the flame diffuses toward the soot layer, leading to this shift in oxidation. However, for this S flame, the magnitude of soot concentrations is greater than can be oxidized and the soot is emitted as noted above.

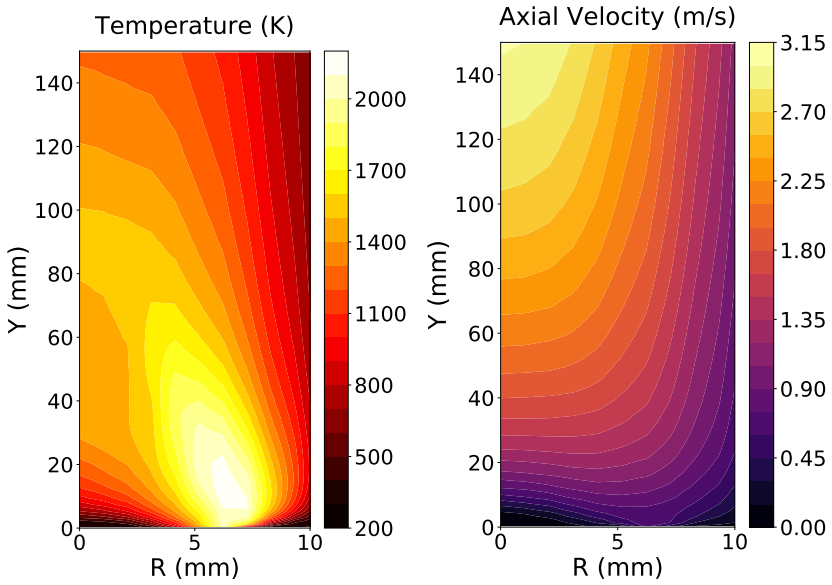

Figure 3-1. Temperature (left) and axial velocity (right) centered around the flame for the 2-D sooting (S) flame.

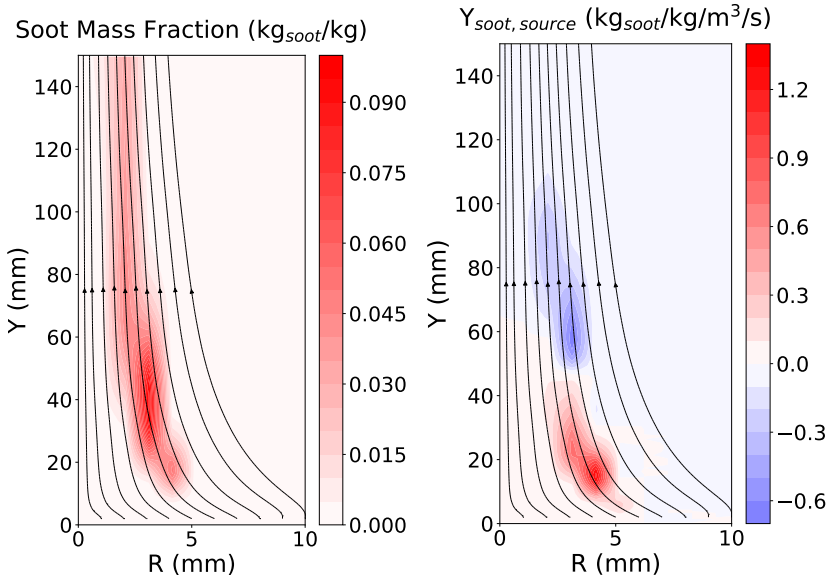

Figure 3-2. Soot mass fraction (left) and soot mass fraction source (right) centered around the flame for the 2-D sooting (S) flame with overlaid stream lines.

3.1.1. 2-D Simulation Validation

The non-sooting case from Santoro et al., Flame NS in Table 2-1, has the largest breadth of data of the range of flow conditions presented and serves as a starting point for comparisons with the simulations [23, 24]. Figure 3-3 shows the axial and radial components of the velocity at a range of elevations versus radial distance from the center of the burner. In general, the predicted axial velocities increase with elevation, following the experiments, with a tendency towards

over-prediction. This acceleration is in agreement with the analysis leading to Eq. 2.14. The largest differences between the predictions and measurements can be seen in the wings of the flame at the lowest elevations (3 mm and 5 mm), while the corresponding peak radial velocities at these elevations are under-predicted. We note that slight asymmetry is present in the experimental flow measurements at the highest elevations.

The overall over-prediction of the buoyant acceleration here might be associated with limitations of the flamelet approach in separating out the soot and mixture fraction. The soot contribution to the density is not included in these simulations as currently implemented. The soot contributions to the enthalpy are also not currently included in determining the gas temperature, and represent another small source of model error that might lead to errors in the buoyant acceleration.

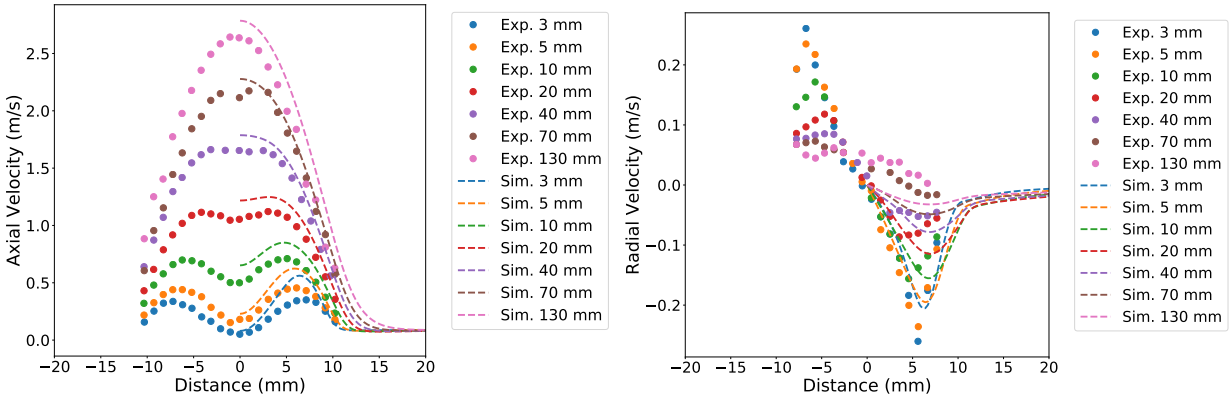

Figure 3-3. Axial (left) and radial (right) velocity comparisons for the non-sooting (NS) case between 2-D simulations (dashes) and experiments (dots) [24].

Temperature comparisons for the non-sooting Flame NS case are shown in Figure 3-4. It is important to note once more that the experimental measurements should be interpreted qualitatively due to the difficulty of correcting thermocouple data in sooting flames. Along the burner centerline, the rate at which the temperature increases with elevation is comparable between simulations and experiments. Similar to the velocity predictions, the largest difference in the temperature evolution occurs in the wings of the flame closest to the burner outlet. In the experiments, the peak temperature increases between measurements at 3 mm and 20 mm whereas the predicted temperatures start high at 3 mm and decrease slightly by 20 mm. These observations corroborate the over-prediction of the axial velocity in the wings at low elevations as higher temperatures generate larger buoyant forces, driving an increase in axial velocity.

The soot volume fraction profiles and the area-integrated soot volume fraction at several elevations from Flame NS are shown in Figure 3-5 for the low flow rate, non-sooting case. Several notable observations can be made from the soot volume fraction profile comparisons in Figure 3-5 (left). At the two higher elevations (50 mm and 82 mm), there is a large under-prediction of soot in the center of the flame. The authors expect that the centerline soot production relies more strongly on larger polycyclic aromatic hydrocarbon molecules that are not included in this present model. The present model relies on acetylene and sufficiently high temperatures for soot production. In the annular region of the flame, peak soot volume fraction predictions are of the same order of magnitude as the measurements with a wider region of

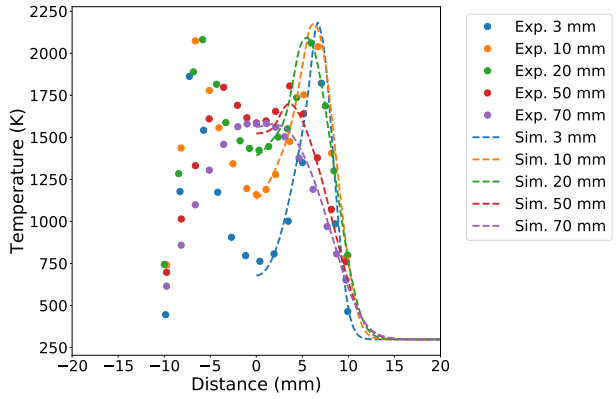

Figure 3-4. Temperature comparisons for the non-sooting (NS) case between 2-D simulations (dashes) and experiments (dots).

predicted soot production at the 15 mm elevation, indicating that soot production is beginning sooner in the simulations than in the experiments. Examining the integrated soot volume fraction versus a non-dimensional height, η, confirms this observation. (An alternative explanation is that early soot formation is not optically accessible because it has not carbonized [9]. Note that η is defined as $yD/\dot{V}$, where y is the elevation above the burner, D is the diffusion coefficient (0.156 cm^2/s), and $\dot{V}$ is the volumetric fuel flow rate.

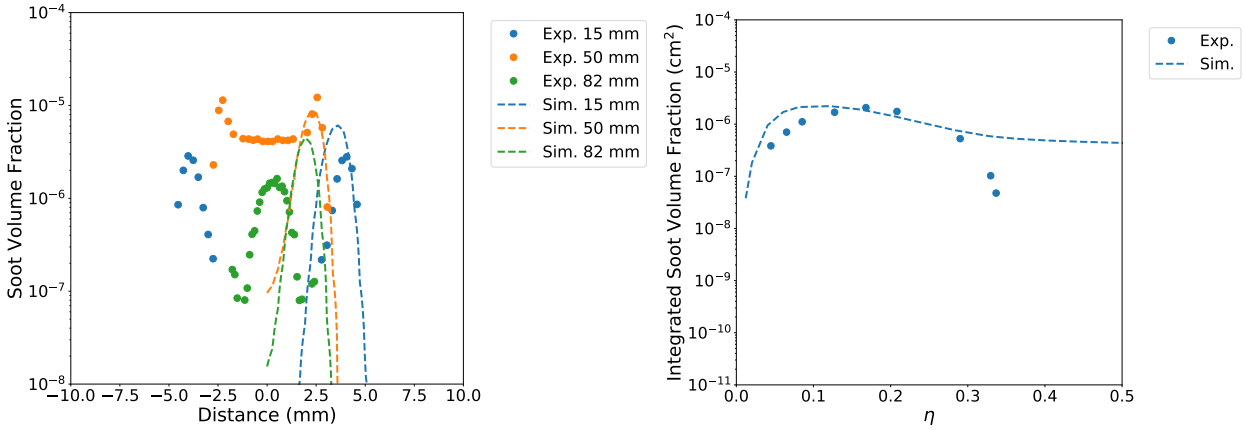

Figure 3-5. Comparison of soot volume fraction at several heights (left) and integrated soot volume fraction versus non-dimensional height, η, (right) for the non-sooting (NS) case between 2-D simulations (dashes) and experiments (dots).

The maximum integrated soot volume fraction production for Flame NS (Fig. 3-5 right) are of the correct magnitude, but the maximum occurs earlier in the simulations than in the experiments. This flame is referred to as the non-sooting case based on experimental observations of soot being consumed below detectable levels in the upper region of the flame, but this sharp drop-off around $\eta \approx 0.3$ is not seen in the simulations.

Full temperature and velocity profiles were not presented in the literature for the sooting case, Flame S in Table 2-1. This flame is one where soot is observed to be emitted from the tip of the flame; it is above the laminar smoke point [18]. Similar to the non-sooting case, predictions of the

peak annular soot volume fraction in the sooting case are on the same order as the measurements as seen in Figure 3-6 (left). The centerline soot volume fraction is under-predicted at each height. Despite these differences, the integrated soot volume fraction exiting the top of the flame aligns with the measurements (Fig. 3-6 right). Based on the integrated soot volume fraction results, it is hypothesized that production and consumption rates peak earlier (at lower elevations) in the simulations than in the experiments.

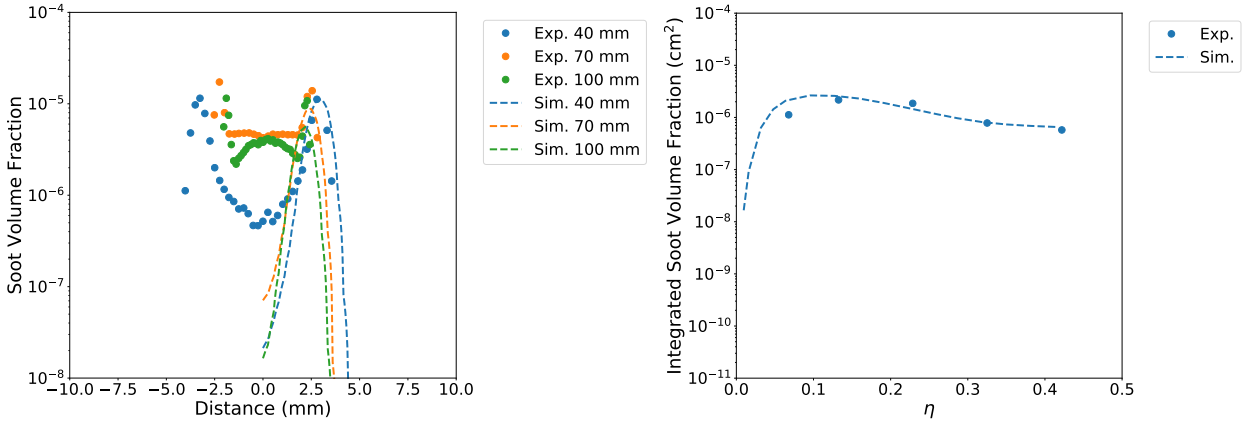

Figure 3-6. Comparison of soot volume fraction at several heights (left) and integrated soot volume fraction versus non-dimensional height, η, (right) for the sooting (S) case between 2-D simulations (dashes) and experiments (dots).

3.1.2. 2-D Versus 3-D Comparisons

Because the majority of simulations are conducted in the fast-running 2-D axi-symmetric configuration, comparisons between several quantities of interest were made between the 2-D axi-symmetric and 3-D simulations depicted in Figure 2-1. The mesh resolution differs and is coarser by a factor of two for the 3-D simulation compared to the 2-D axi-symmetric simulation; the minimum resolution at the fuel inlet is $r_f/10$ for the 3-D simulation and $r_f/20$ for the 2-D simulation where r_f is the fuel inlet radius. The radial temperature profiles for both flow conditions are shown in Figure 3-7. Overall, good agreement can be seen between the 2-D and 3-D simulations for both flow conditions with the largest differences occurring along the centerline. At low elevations, the 2-D centerline temperature predictions are higher than the 3-D predictions, probably because reduced resolution will tend to broaden the profiles where the diffusion is poorly resolved, and predictions from both geometries begin to converge above an elevation of 2 cm. The centerline temperatures in the sooting case are lower than the non-sooting case due to the higher fuel flow rate in the sooting case.

The axial and radial velocities converge between the two geometries with increasing height as seen in Figure 3-8. Similar to the temperature predictions, the largest velocity differences are observed closest to the burner outlet where the 3-D simulation is not as well resolved. At the 3 mm and 5 mm elevations, the peak radial and axial velocities are higher in the 2-D simulations than in 3-D for both flow conditions, and this trend holds for both NS (Fig. 3-8) and S (not shown) flow conditions.

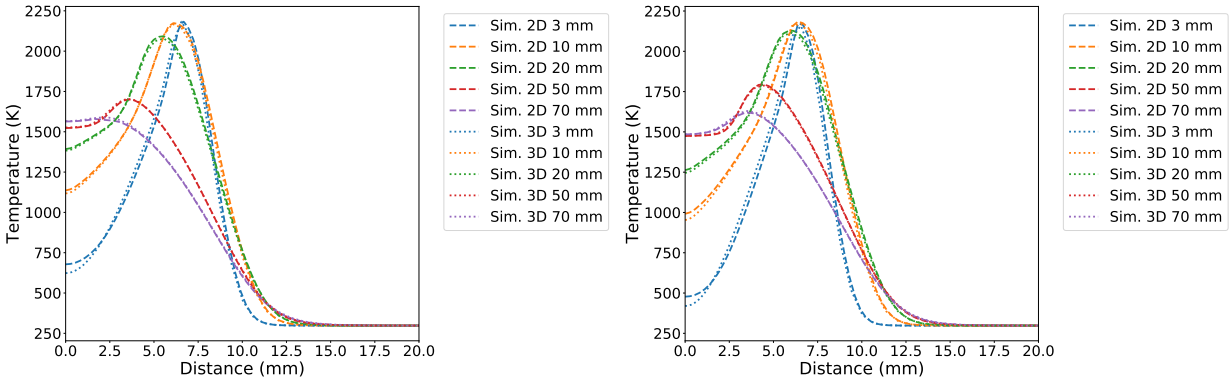

Figure 3-7. Comparison of temperature at several heights between 2-D axi-symmetric (dashed lines) and 3-D (dotted lines) simulations for the NS case (left) and S case (right).

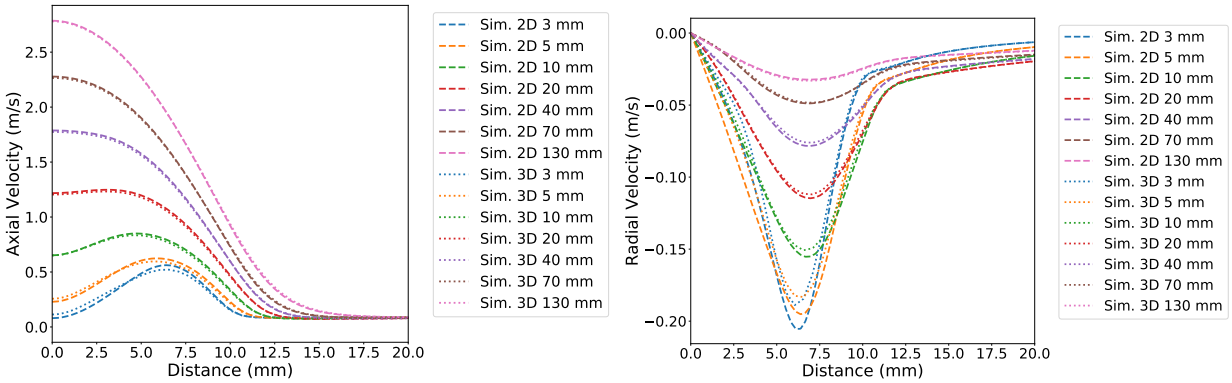

Figure 3-8. Comparison of axial velocity (left) and radial velocity (right) at several heights between 2-D axi-symmetric (dashed lines) and 3-D (dotted lines) simulations for the NS case.

The soot volume fraction and integrated soot volume fraction for both flow conditions and geometries are shown in Figures 3-9 and 3-10. In general, the peak soot volume fractions in the 3-D cases are lower than the 2-D cases, while the profiles are wider in the 3-D simulations due to the coarser mesh (Fig. 3-9). The result is a higher integrated soot volume fraction in the 3-D simulations at low elevations. However, as seen with the other quantities of interest (temperature and velocity), small differences between geometries at low elevations have little effect on the values at higher elevations, and this holds for the total soot production in both flow conditions as seen in Figure 3-10.

The overall results here suggest that the additional resolution that can be applied in the 2-D simulations generally enhances the numerical accuracy. This seems to have only a small effect on the primary quantities of interest that are the overall soot production and subsequent enthalpy evolution.

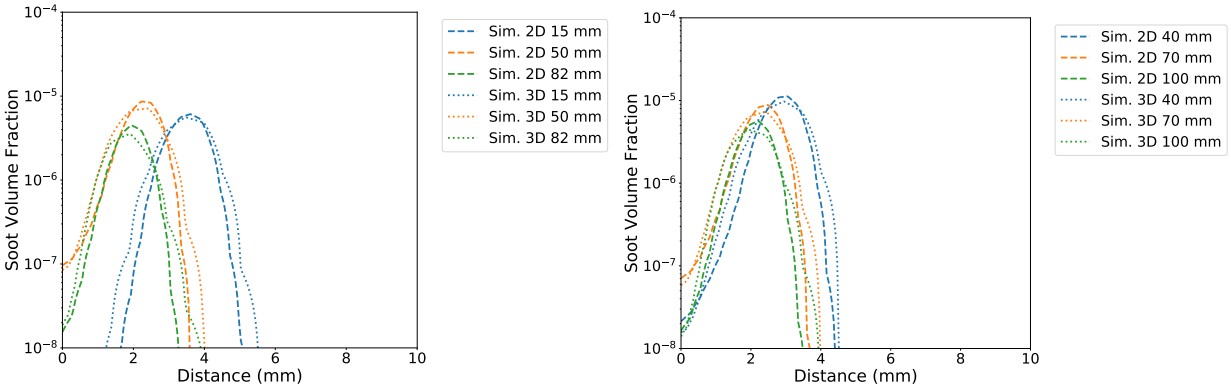

Figure 3-9. Comparison of soot volume fraction at several heights between 2-D axi-symmetric (dashed lines) and 3-D (dotted lines) simulations for the NS case (left) and S case (right).

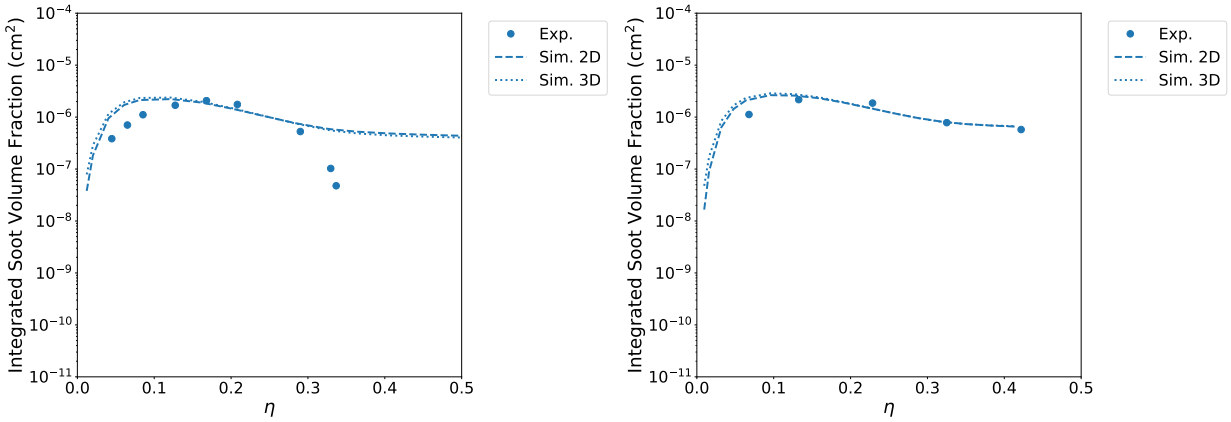

Figure 3-10. Comparison of integrated soot volume fraction at several heights between 2-D axi-symmetric (dashed lines) and 3-D (dotted lines) simulations for the NS case (left) and S case (right).

3.2. Analysis and Discussion

3.2.1. Source Term Comparisons

While the profiles presented in the previous subsections provide detailed results, in order to identify trends over a range of flame conditions, it is helpful to look at integral quantities. To identify appropriate integral quantities, we look at the vertical evolution of the various scalar conservation equations in an area-integrated form as presented in Section 2.5. The area-integrated conservation equations describe the evolution of the vertical flux that differs slightly from the area-integrated soot volume fraction in Figures 3-5, 3-6 and 3-10; those describe the direct area-integrated volume fraction rather than the flux that is described by the conservation equation.

The area-integrated conservation equations generally simplify to

$$\frac{d}{dy}\int_0^\infty \pi\rho u\phi r dr = \int_0^\infty \pi\dot{S} r dr \tag{3.1}$$

where ϕ is the scalar of interest and $\dot{S}$ is the corresponding source term of interest. This describes the change in the flux of ϕ. The units for this evolution when ϕ is like a mass fraction would be kg/m/s while the flux would have units like kg/s. Similarly if ϕ is like an enthalpy, the units of the equation are J/s/m while the flux that is changing is in J/s or W. Conservation of mass and energy provides some overall scale by which we can estimate the magnitude of the different area-integrated evolution terms. For example, the overall flux of mixture fraction plus soot is conserved letting us assess the fraction of total fuel carbon associated with the soot by looking at the ratio of fluxes from Eq. 2.13 and Eq. 2.11. Also, there is a total enthalpy flux with the fuel mass flow rate that gives the (potential) thermal power of the flame; observing the change in this total that can be used to assess radiative loss magnitudes as a fraction of the total heat release.

Figure 3-11 compares the evolution of the two cases described above, NS and S, along with two cases with lower fuel flow rates. Relative to the NS fuel flow rate, the lower rates are reduced by a factor of two and an order of magnitude, indicated here and in the following figures as NS/2 and NS/10, respectively. Note that all analysis in this section was conducted using the 2-D axi-symmetric simulation domain. These flames are shorter by virtue of their lower fuel flow rates; recall flame heights are $H = 0.36\dot{V}/D$ [24]. For the lowest flow rate, the flame is not elongated as depicted in Figures 3-1 and 3-2, but is conical in shape. At these low flow rates the Peclet number is small enough that elliptic terms become important, and upstream diffusion is important. These NS/10 flames have different overall characteristics in terms of the flow field, but are a representative scenario for a low soot limit because the residence times are very short with minimal soot production and minimal radiative losses.

The top panel of Figure 3-11 shows the area-integrated soot volume fraction as presented previously for flames NS and S plotted versus the non-dimensional height (η). The bottom-left panel shows the area-integrated soot flux, the term being differentiated in the axial direction from the left-hand side of Eq. 2.13 and the bottom-right panel depicts the source terms from the right-hand side of Eq. 2.13. In Figure 3-5 it was observed that the soot oxidation at the flame tip

did not fall off as rapidly as measured in the non-sooting case. Here in Figure 3-11 it is seen that the soot profiles do not change dramatically for these various NS simulations in the same manner that they do with the experiments.

One possible reason for slower soot oxidation is greater radiative losses, but as will be seen below, the radiative losses for NS/2 and NS/10 are not large enough to substantially alter OH oxidation. These more dramatic changes in the flame temperature do result in slightly stronger oxidation for the NS/2 and NS/10 cases, but Figure 3-5 shows a sudden order of magnitude reduction in the measured soot when reducing the flow rate slightly from S to NS. This suggests that the model oxidation rate is in disagreement with the measurements [23, 24] and under predicts the oxidation rates.

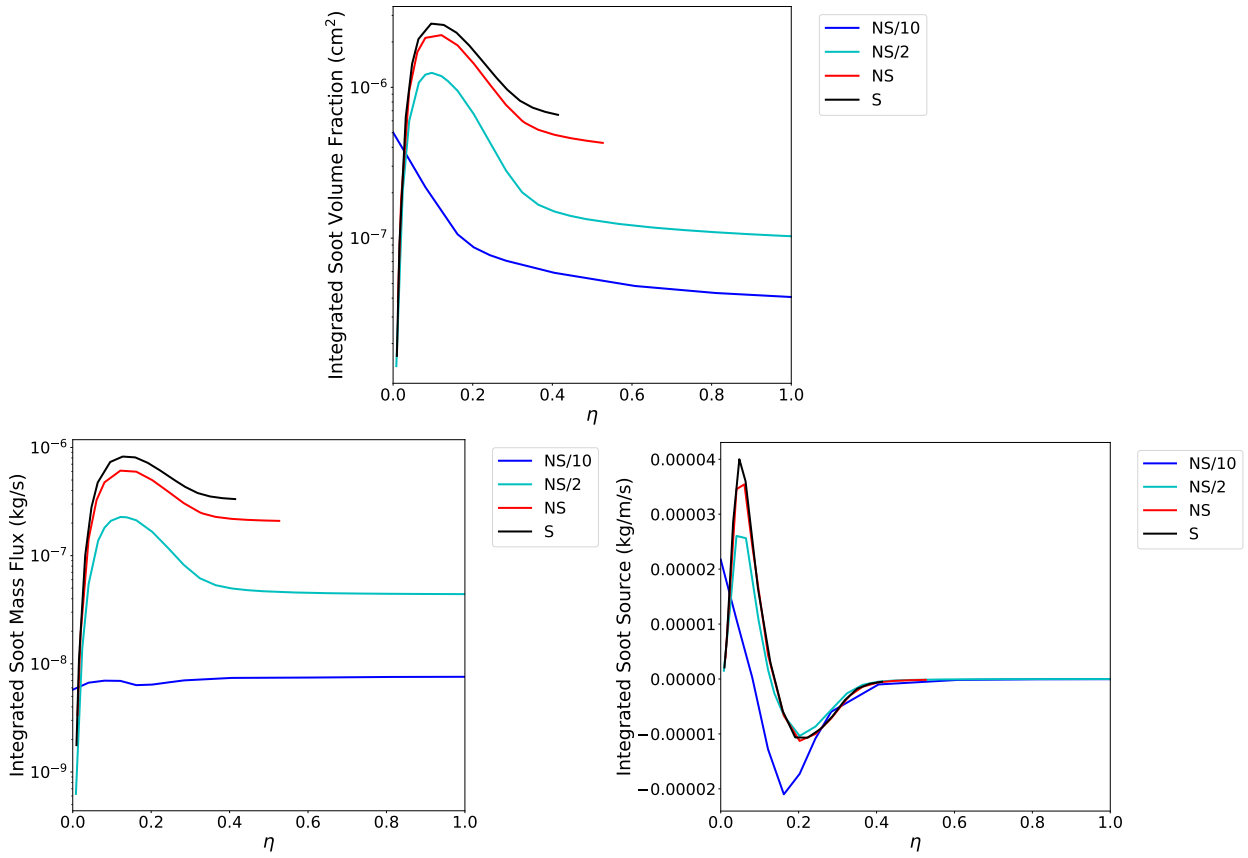

Figure 3-11. Comparison of integrated soot volume fraction (top), integrated soot mass flux (left), and integrated soot mass fraction source (right) versus η between four fuel flow rates: NS/10, NS/2, NS, and S.

To put the integrated soot flux into perspective, it can be normalized by the quantity on the left-hand side of Eq. 2.11 that is the total fuel-mixture flux, a conserved quantity. This quantity is referred to as the soot fraction and is plotted for the four cases in Figure 3-12. The soot fraction of the fuel mass is as high as 15% for the sooting flame, but above the flame tip the soot fraction drops toward 6% and below. While these are reasonable values for the barely sooting flame S, the soot fractions for NS, NS/2 and NS/10 have asymptotic soot fraction magnitudes from 5% to 2%. The normalization by overall fuel flux is an order of magnitude smaller for NS/10 relative to NS,

so even the small quantity of soot in that flame is not negligible. These small flames should emit no soot, reinforcing the deficiencies of the soot oxidation models.

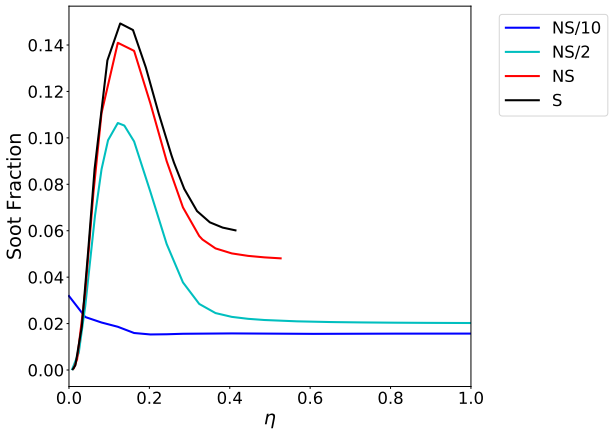

Figure 3-12. Soot fraction versus η between four fuel flow rates: NS/10, NS/2, NS, and S.

Soot production and oxidation are sensitive to radiative heat losses. In Figure 3-13 quantities associated with area-integrated enthalpy evolution as in Eq. 2.12 are plotted. In the left panel, the difference between the left-hand side of Eq. 2.12 and the left-hand side of Eq. 2.11 times the heat of formation of ethylene are used to indicate the heat lost due to radiation. The right-hand panel shows the radiative emission source term on the right-hand side of Eq. 2.12. While the emission is not the complete right-hand side term, these flames are optically thin and absorption is small; absorption is included in the heat-loss plot on the left side.

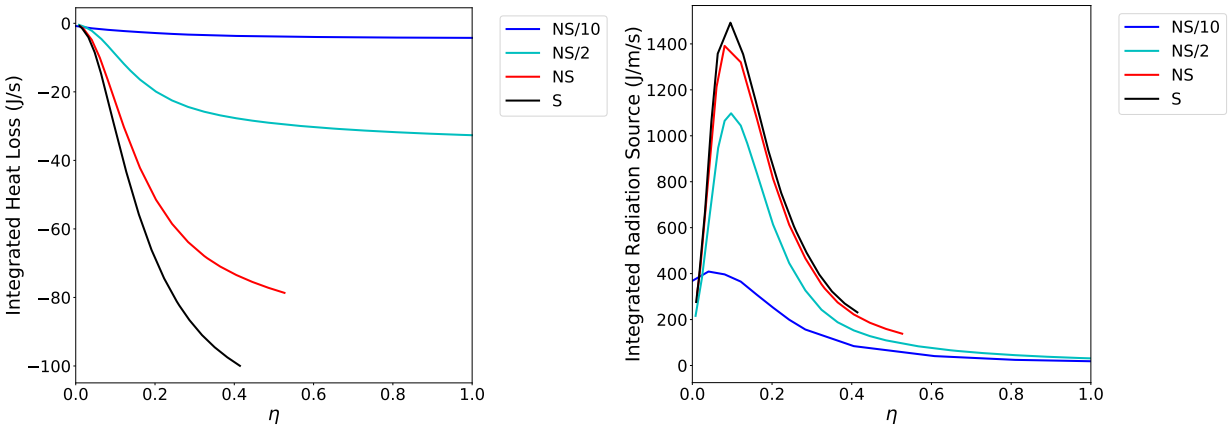

Figure 3-13. Comparison of integrated heat loss (left) and the integrated radiation source (right) versus η between four fuel flow rates: NS/10, NS/2, NS, and S.

To appropriately normalize the heat loss, we divide the integrated heat loss by the total heat of combustion (50 MJ/kg C_2H_4) times the fuel flow rate. This is referred to as the radiant fraction and is plotted in Figure 3-14. Radiative heat losses are greater with greater soot concentrations, but for small flames the relatively slow nature of radiative heat losses can amplify that effect. The radiant fractions range from approximately 15–35% and increase with fuel flow rate and with the soot fraction. For flames with radiative losses on the order of 30% or greater, the main flame

chemistry will weaken and lead to substantial reductions in soot oxidation rates. Radiation cooling does influence the oxidation rates here, but the similar incomplete oxidation from NS/2 and NS/10 suggests poor predictions are associated with the soot oxidation approach employed here.

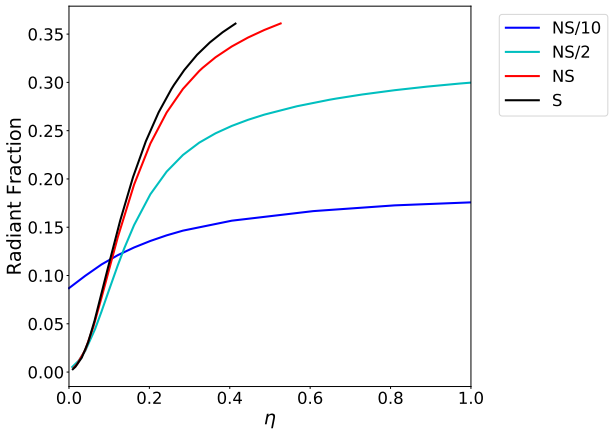

Figure 3-14. Radiant fraction versus η between four fuel flow rates: NS/10, NS/2, NS, and S.

In Figures 3-15 and 3-16, the separated contributions to the various source terms are plotted for the range of flames considered here to better interpret the observations. Of the two soot oxidation pathways in this model, Figure 3-15 shows that the OH soot oxidation pathway is the dominant pathway by at least an order of magnitude. The smallest NS/10 flame does show greater contributions from the O_2 soot oxidation reaction that might arise because this flame has small radiative losses as seen in Figure 3-14. The O_2 oxidation reaction has the largest activation energy in the soot chemistry and is the most temperature sensitive.

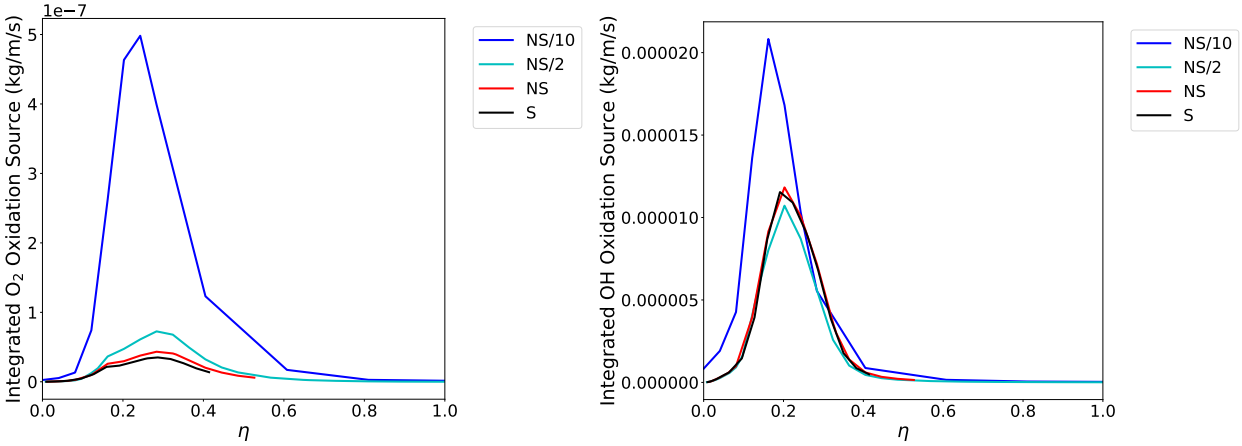

Figure 3-15. Comparison of integrated O_2 oxidation source (left) and OH oxidation source (right) versus η between four fuel flow rates: NS/10, NS/2, NS, and S.

Figure 3-16 shows the contributions of the nucleation model and the surface growth model to the soot production. It is clear that the current nucleation model has a very small contribution to the overall mass of soot produced. These plots also show that the soot production is heavily focused

on the first half of the flame, before $\eta = 0.2$. Apparently, although the flame height is $\eta = 0.36$, the top half of the flame has very little acetylene needed for soot production and is limited to oxidation. Since the OH soot oxidation terms begin to ramp up from the base of the flame, the bottom half of the flame is an environment where both soot production and oxidation are occurring, but soot production is greater up to the point where the sign of the bottom-right integrated soot source in Figure 3-11 switches to negative, generally around $\eta \approx 0.13$ with the exception of the NS/10 case that switches earlier around $\eta \approx 0.08$.

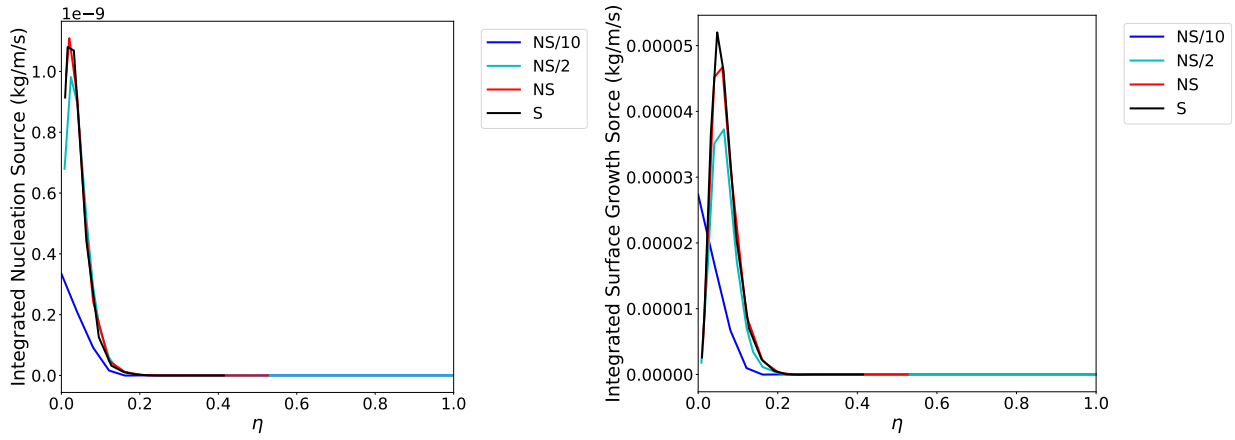

Figure 3-16. Comparison of integrated nucleation source (left) and surface growth source (right) versus η between four fuel flow rates: NS/10, NS/2, NS, and S.

3.2.2. Radial and Centerline Comparisons

For reference, radial profiles of the scalar dissipation rate at two heights are shown in Figure 3-17 for the flames considered here. The two heights are associated with the maximum overall soot production rate and the overall maximum soot oxidation rates. The scalar dissipation rate is relevant to identifying how fast the fuel-air mixing is occurring, and this affects the fraction of carbon conversion to soot. Higher scalar dissipation rates associated with smaller flames lead to smaller fractions of soot conversion, but all of these scalar dissipation rates are on the order of 0.1 s^{-1}, which is fairly small and in a region where soot production is not going to be strongly limited by the fuel-air mixing rate.

Radial and centerline temperature profiles are shown in Figure 3-18 for the range of fuel flow rates. Temperatures along the centerline increase as flow rate decreases due to lower radiative losses at the lowest flow rates as seen in Figures 3-13 and 3-14. These tempearture differences arise because of reduced residence time for soot formation reducing radiative cooling. The difference in the maximum annular temperature between flow rates is less pronounced at lower elevations in the flow after soot production has peaked ($\eta \approx 0.12$).

The soot particle diameter at two heights and along the centerline is displayed in Figure 3-19. The behavior of the particle diameter at the lowest fuel flow rate (NS/10) differs from the three higher flow rate cases. The largest particles are found in the center of the NS/10 flame while the particle size peaks in the annular region of the three larger flames. Analysis from Santoro et al. [23] found

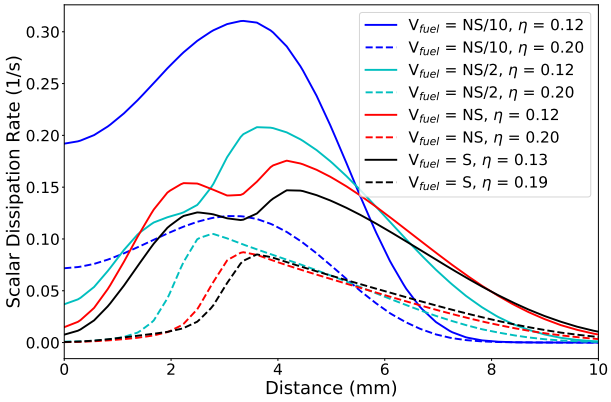

Figure 3-17. Scalar dissipation rate at select heights (η) versus radial distance for four fuel flow rates: NS/10, NS/2, NS, and S.

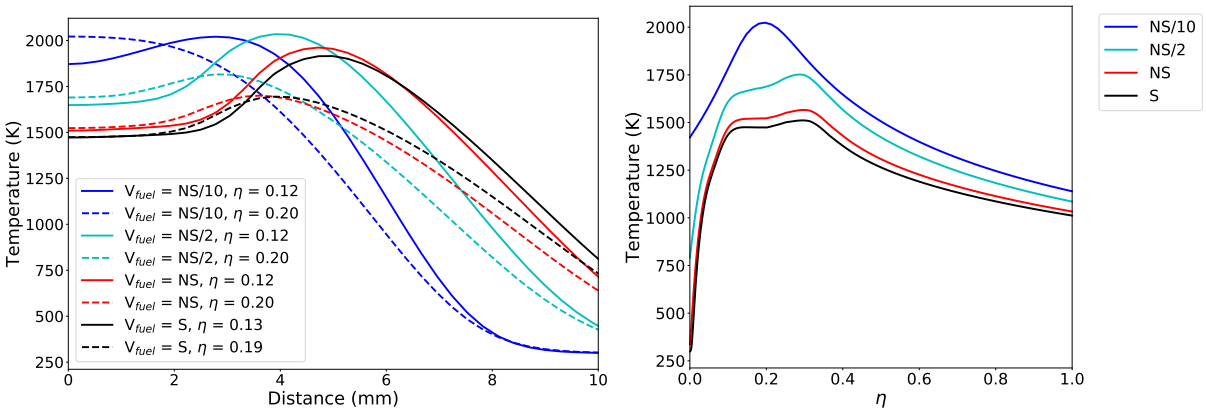

Figure 3-18. Temperature at select heights (η) versus radial distance (left) and along the centerline (right) for four fuel flow rates: NS/10, NS/2, NS, and S.

peak particle sizes on the order of 100 nm in the annular region of NS and S flames. The centerline particle diameter grows beyond the tip of the flame ($\eta \approx 0.36$) in the higher flow rates due to coagulation.

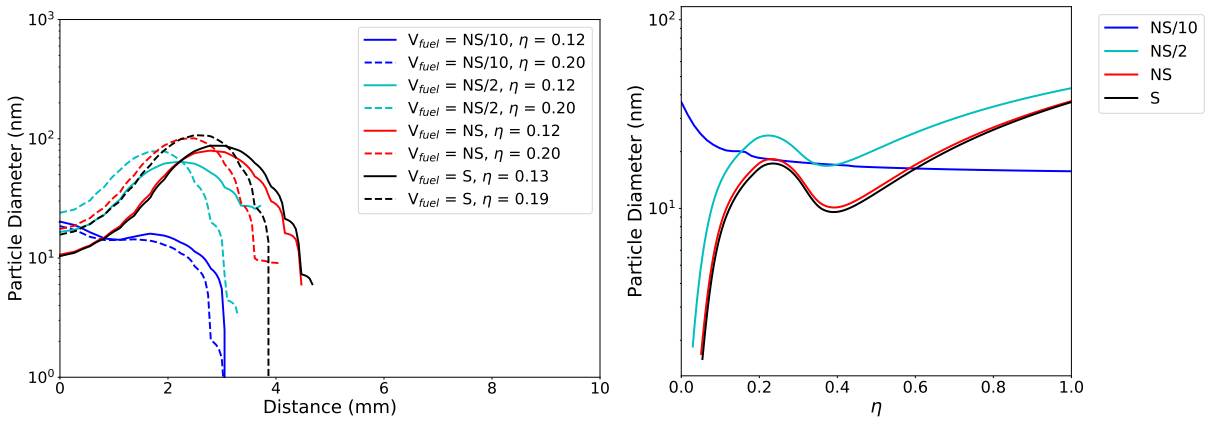

Figure 3-19. Soot particle diameter at select heights (η) versus radial distance (left) and along the centerline (right) for four fuel flow rates: NS/10, NS/2, NS, and S.

3.2.3. *Thermophoretic soot transport*

The predictions developed in the previous sections neglected the thermophoretic contributions to soot transport that are expected to be significant in these laminar flames. A thermophoretic velocity was implemented in Fuego to improve soot transport in the vicinity of the flame sheet. The thermophoretic velocity in direction i ($V_{t,i}$) is modeled as

$$V_{t,i} = -0.554 \frac{\mu}{\rho} \frac{\partial}{\partial x_i} (ln(T)) \tag{3.2}$$

where μ is the gas viscosity, ρ is the mixture density, and T is the local temperature. This term acts to drive soot down the temperature gradient and away from the flame. The resulting thermophoretic velocity, as shown in Figure 3-20 (right), peaks at approximately 10-20% of the maximum radial velocity, assisting the negative radial velocity (Fig. 3-3 right) in shifting the peak soot volume fraction towards the centerline of the flame.

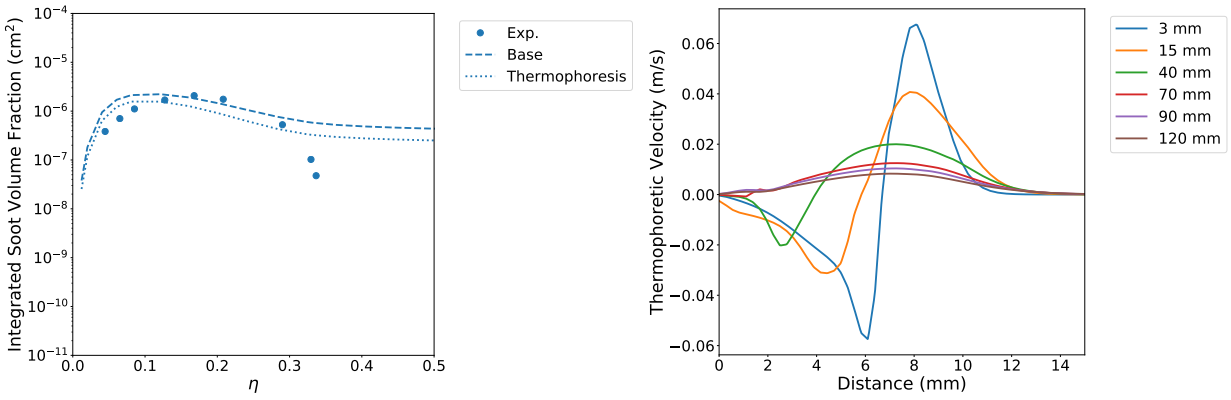

Figure 3-20. Comparison of integrated soot volume fraction at several heights (left) with (dotted lines) and without (dashed lines) thermophoretic velocity enabled for the NS case. Radial component of the thermophoretic velocity at several heights (right).

A small decrease in total soot production over the baseline 2-D model can be seen in the integrated soot volume fraction of the non-sooting simulations (Fig. 3-20 left). An examination of the integrated soot source flux (Fig. 3-21) reveals a decrease in soot production, primarily driven by the soot surface growth source term. More detailed radial profiles are shown in Figures 3-22 and 3-23. With the inclusion of the thermophoretic velocity, the peak soot concentration near the flame sheet decreases and shifts closer to the centerline as the thermophoretic forces drive soot away from the flame sheet. This reduces the surface area available for soot growth, reducing the soot production rate. Thermophoretic transport of the soot away from the highest temperature regions also reduces the radiative losses somewhat as shown in Figure 3-23, which should allow more complete oxidation. However, consumption of the thermophoretically shifted soot particles as they are buoyantly driven towards the top of the flame (around $\eta = 0.35$) is not sufficient to capture the non-sooting behavior observed in the experiments.

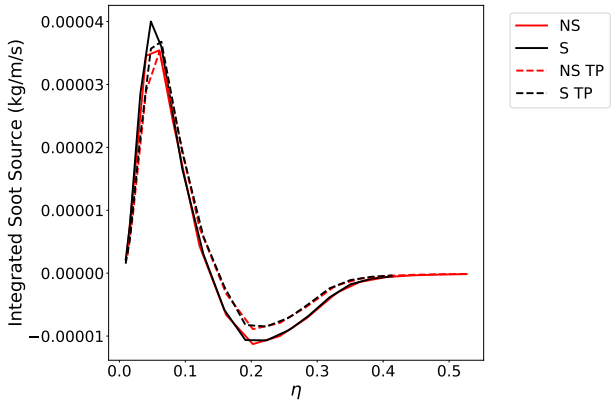

Figure 3-21. Comparison of integrated soot mass fraction source versus η between the base model (solid lines) and thermophoretic (TP) velocity model (dashed lines) for both NS and S flow conditions.

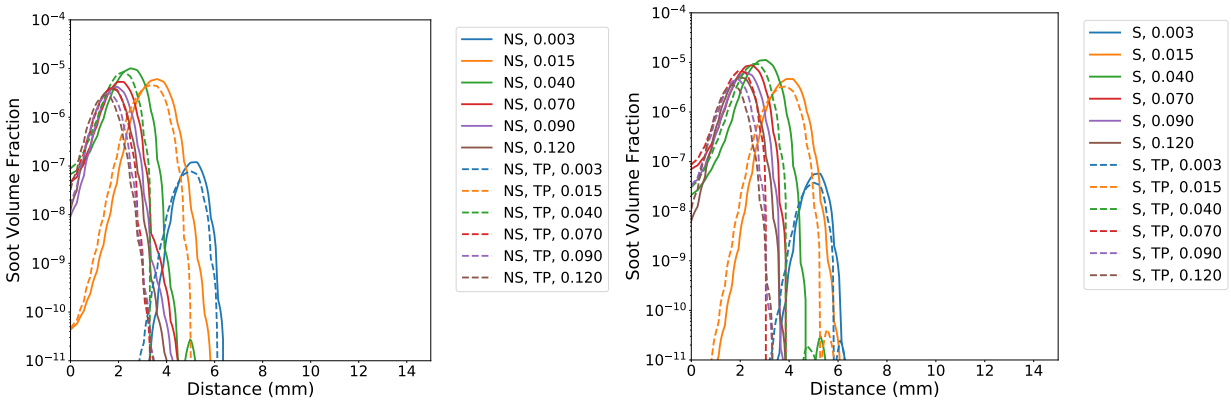

Figure 3-22. Soot volume fraction for the 2-D NS (left) and S (right) flames comparing the base model (solid lines) and thermophoretic (TP) velocity model (dashed lines).

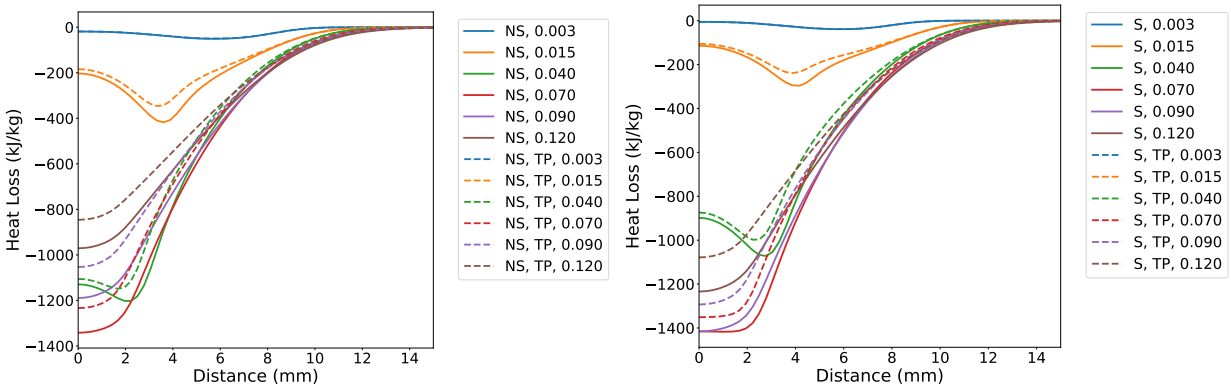

Figure 3-23. Heat loss profiles at several heights for the 2-D NS (left) and S (right) flames comparing the base model (solid lines) and thermophoretic (TP) velocity model (dashed lines).

4. SUMMARY AND CONCLUSION

This report details an assessment of flamelet-based soot models implemented into Fuego through a mixture-fraction based laminar-flamelet model. The model is based on literature source terms that have been developed empirically based on similar measurements and successfully applied for a number of flame simulations. Comparisons of predictions with the velocity and temperature measurements show reasonably good agreement. Soot predictions are also relatively good considering the challenges associated with soot predictions in general, but the simplifications with the current modeling framework do not permit an adequate prediction of the centerline soot, which is under predicted in this approach. This is largely associated with the reliance of this production model on acetylene at higher temperatures; it is expected that the centerline soot depends more strongly on larger polycyclic aromatic hydrocarbons.

Coflow flames and diffusion flames in general can be separated into sooting and non-sooting. For fuel flow rates below some critical smoke-point value the flames are observed to not emit soot, while for fuel flow rates above the critical value soot emissions are observed. The present model for soot oxidation does not predict the sharp transition that has been experimentally observed between sooting and non-sooting flames. For non-sooting conditions, even down to very small flames that should emit no soot at all, soot oxidation at the flame tip seems to be substantially under predicted. This appears to be the greatest discrepancy with the current soot model. The current study is unable to quantify the significance of this for large-scale fire predictions.

Thermophoresis is known to be non-negligible in laminar flames and thermophoretic forcing was added to Fuego and assessed as a part of this study. While the thermophoretic forcing does modestly alter soot production and has a slightly larger influence on the radiative losses, these effects do not markedly influence the predictions or the transition from sooting to non-sooting. In addition to thermophoresis, the effect of 2-D versus 3-D configurations was investigated with the conclusion that the added resolution possible in 2D does slightly improve the predictions in the regions of the highest gradients near the flame base.

The current results suggest that for moderately high sooting levels associated with the transition to sooting, the predictions are reasonable, but for those conditions where soot is expected to be consumed, soot would be emitted in greater quantities in predictions than in reality. This could result in greater smoke shielding of objects low in the fire or in fires with faster mixing (i.e. wind-driven fires).

REFERENCES

[1] I. M. Aksit and J. B. Moss. A hybrid scalar model for sooting turbulent flames. *Combustion and Flame*, 145(1–2):231–244, 2006.

[2] I. M. Aksit and J. B. Moss. Modeling soot formation in a laminar diffusion flame burning a surrogate kerosene fuel. *Proceedings of the Combustion Institute*, 31:3139–3146, 2007.

[3] A. Alexiou and A. Williams. Soot formation in shock-tube pyrolysis of tolune–n-heptane and toluene–iso-octane mixture. *Fuel*, 74(2):153–158, 1995.

[4] ASTM International, West Conshohocken, PA. *ASTM D1322-19. Standard Test Method for Smoke Point of Kerosene and Aviation Fuel*, 2019.

[5] A. Baumgart, J. C. Hewson, T. Voskuilen, and P. Sakievich. Soot and radiation interactions in turbulent jet flames studied with reynolds-averaged navier-stokes simulations, SAND2019-11722C. Technical report, Sandia National Lab.(SNL-NM), Albuquerque, NM (United States), 2019.

[6] S. J. Brookes and J. B. Moss. Predictions of soot and thermal radiation properties in confined turbulent jet diffusion flames. *Combustion and Flame*, 116:486–503, 1999.

[7] P. Chatterjee, J. L. de Ris, Y. Wang, and S. B. Dorofeev. A model for soot radiation in buoyant diffusion flames. *Proceedings of the Combustion Institute*, 33:2665–2671, 2011.

[8] P. Chatterjee, J. L. de Ris, Y. Wang, N. Krishnamoorthy, and S. B. Dorofeev. *Laminar Smoke Point Based Subgrid Soot Radiation Modeling Applied to LES of Buoyant Turbulent Diffusion Flame*, volume 369 of *Journal of Physics Conference Series*. 2012.

[9] R. A. Dobbins. Soot inception temperature and the carbonization rate of precursor particles. *Combust. Flame*, 130:204–214, 2002.

[10] S. P. Domino, J. C. Hewson, R. Knaus, and M. A. Hansen. Predicting large-scale pool fire dynamics using an unsteady flamelet and large-eddy simulation-based model suite. *Phys. Fluids*, 2021.

[11] Stefan Domino. Sierra Low Mach Module: Nalu Theory Manual 1.0, SAND2015-3107W. Technical report, Sandia National Laboratories Unclassified Unlimited Release (UUR), https://github.com/NaluCFD/NaluDoc, 2015.

[12] Seth B Dworkin, Qingan Zhang, Murray J Thomson, Nadezhda A Slavinskaya, and Uwe Riedel. Application of an enhanced PAH growth model to soot formation in a laminar coflow ethylene/air diffusion flame. *Combustion and Flame*, 158(9):1682–1695, 2011.

[13] M. Fairweather, W. P. Jones, and R. P. Lindstedt. Predictions of radiative transfer from a turbulent reacting jet in a cross-wind. *Combustion and Flame*, 89(45–63), 1992.

[14] M. Frenklach, S. Taki, M. B. Durgaprasad, and R. A. Matula. Soot formation in shock tube pyrolysis of acetylene, allene and 1,3-butadiene. *Combustion and Flame*, 54:81–101, 1983.

[15] S. P. Kearney and T. W. Grasser. Laser diagnostic mapping of temperature and soot statistics in a 2-m diameter turbulent pool fire. *Combustion and Flame*, 186:32–44, 2017.

[16] Kin M Leung, Rune P Lindstedt, and William P Jones. A simplified reaction mechanism for soot formation in nonpremixed flames. *Combustion and Flame*, 87(3-4):289–305, 1991.

[17] Fengshan Liu, Hongsheng Guo, Gregory J Smallwood, and Ömer L Gülder. Numerical modelling of soot formation and oxidation in laminar coflow non-smoking and smoking ethylene diffusion flames. *Combustion Theory and Modelling*, 7(2):301, 2003.

[18] G. H. Markstein. Relationship between smoke point and radiant emissions from buoyant and laminar diffusion flames. In *The Twentieth Symposium (International) on Combustion*, pages 1055–1061. The Combustion Institute, Pittsburgh, 1984.

[19] J. B. Moss and C. D. Stewart. Flamelet-based smoke properties for the field modelling of fires. *Fire Safety Journal*, 30(3):229–250, 1998.

[20] J. Murphy and C. Shaddix. Soot property measurements in a two-meter diameter JP-8 pool fire. *Combustion Science and Technology*, 178:865–894, 2006.

[21] N. Peters and J. Göttgens. Scaling of buoyant turbulent jet diffusion flames. *Combustion and Flame*, 85:206–214, 1990.

[22] F. G. Roper. The prediction of laminar jet diffusion flame sizes: Part I. theoretical model. *Combustion and Flame*, 29:219–226, 1977.

[23] RJ Santoro, HG Semerjian, and RA Dobbins. Soot particle measurements in diffusion flames. *Combustion and Flame*, 51:203–218, 1983.

[24] RJ Santoro, TT Yeh, JJ Horvath, and HG Semerjian. The transport and growth of soot particles in laminar diffusion flames. *Combustion Science and Technology*, 53(2-3):89–115, 1987.

[25] Christopher R Shaddix and Kermit C Smyth. Laser-induced incandescence measurements of soot production in steady and flickering methane, propane, and ethylene diffusion flames. *Combustion and flame*, 107(4):418–452, 1996.

[26] SIERRA Thermal/Fluid Development Team. SIERRA Low Mach Module: Fuego Theory Manual – Version 5.0, SAND2021-3929. Technical report, Sandia National Laboratories, March 2021.

[27] SIERRA Thermal/Fluid Development Team. SIERRA Low Mach Module: Fuego User Manual – Version 5.0, SAND2021-3928. Technical report, Sandia National Laboratories, March 2021.

[28] P. A. Tesner, T. D. Snegiriova, and V. G. Knorre. Kinetics of dispersed carbon formation. *Combustion and Flame*, 17:253–260, 1971.

[29] A. Tewarson. Smoke point height and fire properties of materials. nist-gcr-88-555. Report, Nat. Instit. Stand. Tech., 1988.

[30] Z. Wen, S. Yun, M. J. Thompson, and M. F. Lightstone. Modeling soot formation in turbulent kerosene/air jet diffusion flames. *Combustion and Flame*, 135:323–340, 2003.

[31] Timothy C Williams, Christopher R Shaddix, Kirk A Jensen, and Jill M Suo-Anttila. Measurement of the dimensionless extinction coefficient of soot within laminar diffusion flames. *International Journal of Heat and Mass Transfer*, 50(7-8):1616–1630, 2007.

[32] J. J. Young and J. B. Moss. Modeling sooting turbulent jet flames using an extended flamlet technique. *Combustion Science and Technology*, 105:33–53, 1995.

DISTRIBUTION

Email—Internal [redacted]

Name	Org.	Sandia Email Address
Technical Library	1911	sanddocs@sandia.gov

Sandia National Laboratories

Sandia National Laboratories is a multimission laboratory managed and operated by National Technology & Engineering Solutions of Sandia LLC, a wholly owned subsidiary of Honeywell International Inc., for the U.S. Department of Energy's National Nuclear Security Administration under contract DE-NA0003525.